Sn-O Dual-substituted Chlorine-rich Argyrodite Electrolyte with Enhanced Moisture and Electrochemical Stability

Guoyao Li[a], Shaoping Wu[a], Hongpeng Zheng[a], Yu Yang[b], Jingyu Cai[a], Hong Zhu[b], Xiao Huang[c], Hezhou Liu[a], Huanan Duan[a]*

[a]G. Li, S. W, H. Zheng, J. Cai, H. Liu, H. Duan*

State Key Laboratory of Metal Matrix Composites, School of Materials Science and Engineering, Shanghai Jiao Tong University, Shanghai 200240, P. R. China

E-mail: hd1@sjtu.edu.cn

[b]Y. Yang, H. Zhu

University of Michigan-Shanghai Jiao Tong University Joint Institute, Shanghai Jiao Tong University, Shanghai 200240, P. R. China

[c]X. Huang

SZU-NUS Collaborative Innovation Center for Optoelectronic Science & Technology, International Collaborative Laboratory of 2D Materials for Optoelectronics Science and Technology of Ministry of Education, Institute of Microscale Optoelectronics, Shenzhen University, Shenzhen 518060, P. R. China

ABSTRACT

Chlorine-rich argyrodite sulfides are one of the most promising solid electrolytes for

all-solid-state batteries owing to their remarkable ionic conductivity and decent mechanical

properties. However, their application has been limited by imperfections such as moisture

instability and poor electrochemical stability. Herein, we propose a Sn and O

dual-substitution strategy in $Li_{5.4}PS_{4.4}Cl_{1.6}$ (LPSC) to improve the moisture tolerance and

boost the electrochemical performance. The optimized composition of

$Li_{5.5}(P_{0.9}Sn_{0.1})(S_{4.2}O_{0.2})Cl_{1.6}$ (LPSC-10) sintered at 500 °C exhibits a room-temperature ionic

conductivity of 8.7 mS cm^{-1}, an electrochemical window up to 5 V, a critical current density

of 1.2 mA cm^{-2}, and stable lithium plating/striping. When exposed to humid air, LPSC-10

exhibits a small increment in total resistance, generates a mild amount of H_2S gas, and

displays favorable structure stability after heat treatment. The first-principles calculation

confirms that the dual-substituted composition less tends to be hydrolyzed than the

un-substituted one. The all-solid-state battery with LiIn|NMC811 electrodes presents a high

initial discharge capacity of 103.6 mAh g^{-1} at 0.5 C rate and maintains 101.4 mAh g^{-1} at the

100th cycle, with a 97.9% capacity retention rate. The present work opens a new alternative

for simultaneously promoting moisture and electrochemical stability.

2

1. Introduction

The rapid development of electric vehicles has put forward unprecedented requirements for lithium-ion batteries (LIBs). To meet the demands on high energy density and working safety simultaneously, extensive research efforts have been dedicated to developing all-solid-state lithium batteries (ASSLBs) with key materials of solid electrolytes (SEs) [1]. Among various types of SEs, sulfides stand out on account of their prominent ionic conductivity [2] and decent formability [2d, 3]. For instance, the ionic conductivity of the representative sulfide SEs like $70Li_2S-30P_2S_5$[2a], $Li_{10}GeP_2S_{12}$[2b], $Li_{9.54}Si_{1.74}P_{1.44}S_{11.7}Cl_{0.3}$[2c] and $Li_{5.4}PS_{4.4}Cl_{1.6}$ (argyrodite type) [2d], reaches 17, 25, 12 and 8.4 mS cm^{-1}, respectively, comparable to that of the liquid SEs. Argyrodite-type sulfides, in particular, win a competitive edge over other sulfides because no self-accelerated interfacial reaction with lithium metal occurs [4] and no costly raw materials are employed [5]. Therefore, Li argyrodites have been considered to be one of the most attracting SEs. The halogen elements in argyrodites Li_6PS_5X (X = Cl, Br, and I) largely affect the Li-ion conduction via introducing different degrees of X^-/S^{2-} disorder; the chlorine-containing argyrodite exhibits the highest ionic conductivity owing to the largest degree of the X^-/S^{2-} disorder among the halogen elements [6]. Moreover, chlorinity plays an important role in determining ionic conductivity -- the more the chlorine, the higher the conductivity [7]. As a result, $Li_{5.4}PS_{4.4}Cl_{1.6}$, a chlorine-rich argyrodite, has been reported to achieve a high ionic conductivity of 8.4 mS cm^{-1} [2d]. It can also be processed into an ultrathin film with a thickness of 30 μm, which shows great promise for future ASSLB applications.

However, two main issues have plagued the development of argyrodite-based ASSLBs. Firstly, Li argyrodite exhibits poor resistance to H_2O [8]. Due to the high oxygen affinity of

P^{5+} in argyrodites, H_2O can easily attack the weak P-S bonding in a humid environment and generate toxic H_2S gas. The reaction with H_2O will deviate the composition and structure, and severely impair the electrochemical performance of argyrodites [8-9]. Secondly, theoretical [10] and experimental [11] results show that Li argyrodites have a narrow electrochemical window (< 2.2 V), so it is challenging to realize the interfacial stability when argyrodites are integrated into ASSLBs [1c, 12], especially when matching with the lithium anode [4a, 7, 13] and high-voltage cathode [14]. Therefore, it is of great significance to improve the moisture stability of the argyrodites and enhance their lithium-anode compatibility without sacrificing ionic conductivity.

Considerable efforts have been made to develop strategies to mitigate the moisture sensibility of argyrodites. One method is to add porous materials that can absorb H_2S or H_2O molecules. For instance, Lee et al. introduced zeolites into Li_6PS_5Cl and effectively slowed the H_2S generation rate [15]. However, such a composite electrolyte is not intrinsically stable to moisture since it could not eliminate the reaction between the argyrodite and moisture. Another method is element substitution. Oxygen substitution of sulfur has been verified to enhance the structural stability of argyrodites in humid air, such as $Li_6PS_{5-x}O_xCl$ [16] and $Li_6PS_{5-x}O_xBr$ [17]. The enhancement can be attributed to the high chemical stability of oxide electrolytes by forming oxysulfide [8]. However, too much oxygen substitution will dramatically decrease the ionic conductivity. An empirical guide for element substitution is the so-called "hard and soft acids and bases (HSAB)" theory, which states that soft (easily polarizable) acids preferentially react with soft bases, and hard (non-polarizable) acids tend to react with hard bases. For example, Sahu et al. substituted hard acid, phosphorus, with soft acid elements, Sn and As, because the soft acid is prone to form stable compounds with the soft base, sulfur [18]. Indeed, the As-substituted Li_4SnS_4 demonstrated superior air stability.

4

The soft acid substitution strategy has set off a wave of development of air-stable sulfide SEs like Sn-substituted Li_6PS_5I [19] and In-substituted Li_6PS_5I [20]. In addition, due to the aliovalent substitution or larger radius of these soft acid atoms, the substituted argyrodites can even deliver enhanced ionic conductivity.

Meanwhile, possible strategies to alleviate the interfacial incompatibility of argyrodites with lithium-metal anode are also presented, which can be divided into two main categories. One is to design an interlayer that is characteristic of intrinsic stability to lithium metal to physically separate lithium from argyrodites. The interlayers are mainly inorganic substances such as graphite [21], alumina oxide [2d], and silver-carbon composite [22]. Nevertheless, such an interlayer not only requires tedious fabrication but also brings uncertainty in thickness. The other category is via element substitution in argyrodites. The representative elements like N [23], F [24], and I [25] enable the sulfide SEs to in-situ form SEI film with the composition of Li_3N, LiF, and LiI, respectively, when contacting with the lithium anode and cycling. These SEI components have been reported to stabilize the interfacial evolution and facilitate uniform lithium deposition and stripping [25-26]. Furthermore, it is worth noting that oxygen or soft acid substitution aimed at promoting moisture stability can also boost the lithium-compatibility [27]. It can be summarized that element substitution is a feasible and versatile method to design argyrodite sulfides with homogeneous composition, structure, properties, and even multi-functions.

Here, we aim to use a dual-substitution strategy of Sn and O elements to simultaneously promote the moisture and electrochemical stability of the chlorine-rich argyrodite sulfide $Li_{5.4}PS_{4.4}Cl_{1.6}$ (LPSC). The chemical composition and structure of the dual-substituted sample were systematically studied. The influencing factor of ionic conductivity like the substitution amount and sintering temperature was also investigated. Consequently, the dual-substituted

sample with a 10% substitution level (LPSC-10) sintered at 500 ℃ possesses the highest

ionic conductivity and critical current density with an electrochemical window as large as 5 V

versus Li/Li$^+$. Subsequently, LPSC-10 was verified with enhanced moisture stability

according to a series of humid-air-exposed tests as well as first-principles calculation. The

LiIn|LPSC-10|NMC811 battery was finally fabricated to demonstrate its applicability in

energy storage.

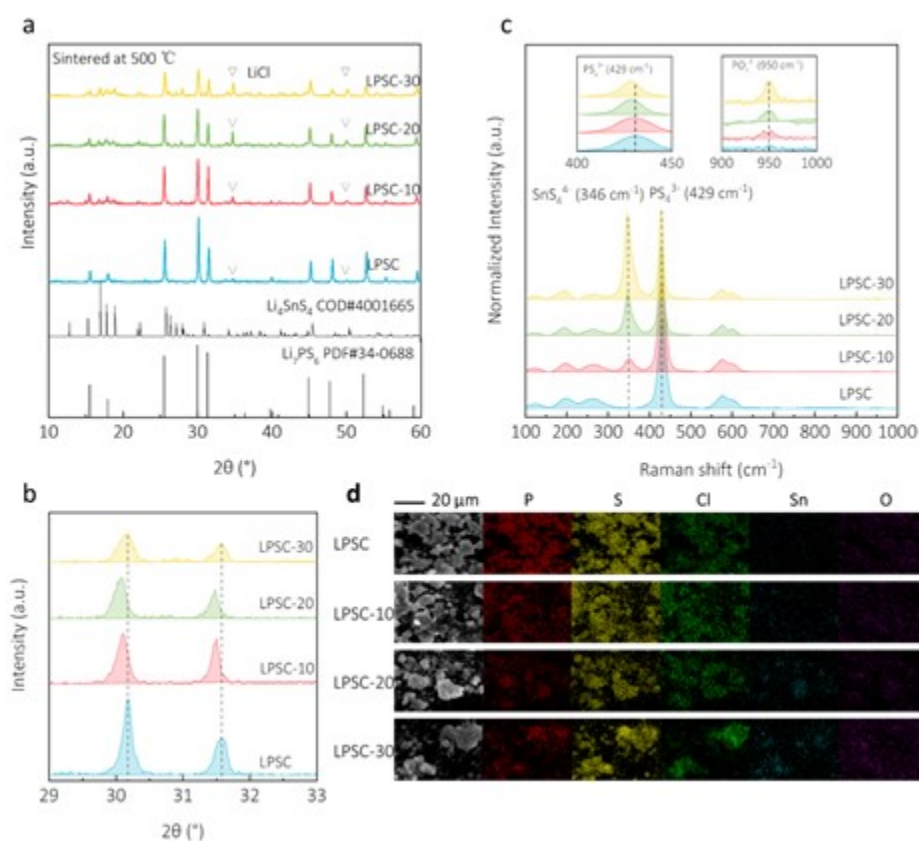## 2. Results and Discussion

Figure 1. Characterization of the chemical composition and structure of the sulfide samples
sintered at 500 ℃. (a) The powder XRD patterns of the samples, the referenced pattern of the

secondary phase Li_4SnS_4 (source: Crystallography Open Database), and the standard PDF of the argyrodite sulfide prototype Li_7PS_6. (b) The magnified view of the XRD patterns spotted among 29°-33° of the graph (a). (c) The Raman spectroscopy of the samples. (d) The SEM images and EDS mapping of the samples.

The phase evolution of the 500 °C-sintered samples was investigated by the powder X-ray diffraction shown in Figure 1a. The primary diffraction peaks of sulfide samples agree well with the cubic argyrodite-type structure (F-43m space group. See the Rietveld refinement results in Figure S1 and Table S1), indicating the successful synthesis of the desired sulfide. Close inspection of the minor peaks around 35° and 50° suggests that a trace amount of LiCl phase exists, which is a common impurity for chlorine-rich LPSC [28]. As the substitution amount increases, the residual amount of the LiCl phase rises evidently; so does the secondary phase of Li_4SnS_4[29]. The appearance of Li_4SnS_4 can be attributed to the competitive reaction between the formation of Li_4SnS_4 and the Sn-O substituted primary phase. On one hand, the Sn^{4+} can substitute the P^{5+} at the 4b site in the argyrodite lattice; on the other hand, the substitution amount is limited due to the Sn^{4+}/P^{5+} radius difference, determining the solubility limit of Sn^{4+} in LPSC [19]. Excess SnS_2 dopant is prone to form a $2Li_2S$-SnS_2 binary system or Li_4SnS_4 phase, simultaneously increasing the residual amount of LiCl phase in the dual-substituted samples. The more the SnS_2 dopant, the higher the impurity (i.e., Li_4SnS_4 and LiCl) level.

The substitution of Sn and O was further identified in the magnified XRD results with the 2θ angle at 29-33°, as shown in Figure 1b. When the substitution amount increases, the primary diffraction peaks of the dual-substituted phase shift towards a small angle for LPSC-10 and LPSC-20, and back to a large angle for LPSC-30, indicating that the lattice

expands first and then contracts. This shift can be due to the different solubility of Sn and O in the argyrodite lattice. For the aliovalent substitution of P^{5+} with Sn^{4+}, owing to the larger ion radius of Sn^{4+} (69 pm) than that of P^{5+} ion (38 pm) and the large radius difference that restrains the Sn solubility, the introduction of Sn^{4+} will expand the lattice with a low dopant level [30]. However, for substitution of S^{2-} with O^{2-}, owing to the smaller ion radius of O^{2-} (140 pm) than that of S^{2-} ion (184 pm) and the O affinity to the P element that contributes to relatively large solubility of O, the introduction of O will constrict the lattice within a high dopant level [31]. In another word, the lattice expansion associated with Sn substitution is dominant in low-dopant-level samples like LPSC-10 and LPSC-20; whereas in high-dopant-level samples like LPSC-30, the lattice constriction associated with O substitution plays a leading role, so the overall lattice shrinks.

Raman spectroscopy was performed to characterize the chemical groups like PS_4^{3-}, SnS_4^{4-} and PO_4^{3-} in sulfide samples. All the peaks were normalized to the strongest peak with a wavenumber of 429 cm^{-1}. As shown in Figure 1c, the peak with a wavenumber of 429 cm^{-1} is attributed to the symmetric vibration mode of an ortho-thiophosphate group, PS_4^{3-}. The peaks with wavenumbers of 197 and 265 cm^{-1}, as well as 577 and 603 cm^{-1}, can be attributed to the deformation vibration and asymmetric stretching vibration of PS_4^{3-}, respectively [32]. As the substitution amount rises, new peaks arise with wavenumbers of 346 cm^{-1} and 950 cm^{-1} (depicted in the inset of Figure 1c), which can be assigned to SnS_4^{4-}[33] and PO_4^{3-}[34], respectively. The existence of the SnS_4^{4-} group is aligned with the XRD results in Figure 1a, verifying the formation of the secondary phase of Li_4SnS_4. The relative intensity of the SnS_4^{4-} peak increases monotonically with increasing substitution amount, reflecting the increasing amount of the Li_4SnS_4 phase; meanwhile, the amount of the PO_4^{3-} group also rises. Besides, the inset of Figure 1c shows that the principal peak of the PS_4^{3-} group at 429 cm^{-1} shifts to the

lower band (red-shift) via dual substitution, which is mainly associated with the lattice expansion by Sn substitution [30], consistently with the XRD results in Figure 1b. Taklu, et al. have reported a similar shifting behavior in Raman spectroscopy and attributed the shift to the lattice expansion in the Cu-substituted argyrodite sulfide [35]. It can be inferred that when Sn and O atoms partly replace the P and S in the principal PS_4^{3-} group, respectively, it will not result in the change of vibration mode of PS_4^{3-}, but a peak shift.

Furthermore, the effect of the dopant source, i.e. SnO_2 dopant and dual-dopant (combination of SnS_2 and P_2O_5), on the phase formation was studied via XRD and Raman measurements. The molar ratio of Sn and O atoms in the SnO_2-dopant samples was controlled to be identical to that in the dual-dopant samples. As shown in Figure S2, compared with the unsubstituted LPSC, a sharp diffraction peak that is attributed to some unknown impurity emerges at 15° for LPSC-10SnO_2, and declines for LPSC-20SnO_2 and LPSC-30SnO_2. In particular, for LPSC-30SnO_2, the peak intensity of the primary phase drops drastically, indicating a decreased crystallinity or phase proportion of the dual-substituted sulfide. The Raman results in Figure S3 show that for LPSC-30SnO_2, the peak intensity of the SnS_4^{4-} group dramatically rises to exceed that of the PS_4^{3-} group; meanwhile, there occur some undesired vibration peaks at 215, 275, and 400 cm^{-1}, which can be attributed to the residual SnO_2 and its related byproducts [36]. It can be concluded that the SnO_2 dopant leads to more heterogeneity in chemical composition, rendering more impurity phases. Thus, the dual-dopant was adopted for the present work.

The morphology of sulfide samples and the element distribution were investigated by SEM and EDS mapping. As shown in Figure 1d, the sulfide particles present a rising size, up to 10 μm for LPSC-30, implying that the formability or softness of the sulfides is weakened with increasing substitution amount. It is well known that compared with O^{2-}, S^{2-} possesses a

larger ion radius and is less electronegative, endowing sulfide electrolyte inherent softness [37]. In other words, the introduction of O substitution in the sulfide framework compromises its formability or softness. As for the element distribution, the EDS mapping confirms the homogeneous distribution of each component element in $Li_{5.4+x}(P_{1-x}Sn_x)(S_{4.4-2x}O_{2x})Cl_{1.6}$. The signals of Sn and O elements rise with increasing Sn and O substitution. It is also noted that a non-negligible amount of O element occurs in the unsubstituted LPSC, which is probably due to the short-time air exposure when the sample was transferred into the vacuum chamber of the SEM, suggesting the poor air stability of the pristine sample.
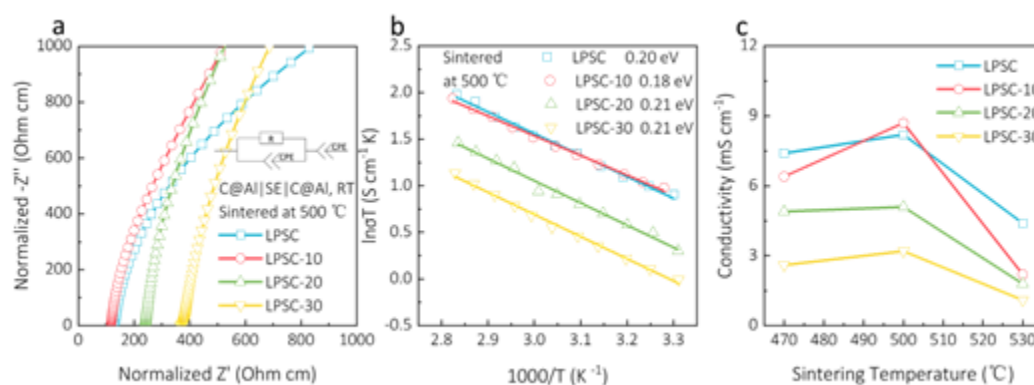

Figure 2. Effect of the dual substitution and sintering temperature on the ionic conductivity of the cold-pressed sulfide samples. (a) The Nyquist plots of the pelletized samples sintered at 500 °C, where the impedance is normalized to the respective pellet geometry. The inset presents the equivalent circuit (R//CPE)-CPE (b) The Arrhenius plots of the pelletized samples sintered at 500 °C, measured at a temperature range of 303-353 K with an interval of 5 K. (c) The ionic conductivity of the pelletized samples sintered at 470, 500, and 530 °C.

The ionic conductivity of the as-prepared sulfide samples was characterized by electrochemical impedance spectroscopy (EIS). Figure 2a depicts the EIS plots of the sulfide

10

samples sintered at 500 °C. Normally, the Nyquist plot of solid electrolyte consists of a semicircle at a high-frequency region together with an inclined tail at a low-frequency region, corresponding to the bulk transport (including bulk and grain boundary) and the effect using an ion-blocking electrode, respectively [38]. Whereas in Figure 2a, only the inclined tail was found; the semicircle is absent, which is typically observed for the argyrodite sulfides with ultrahigh ionic conductivity [39]. Karft, et al. have pointed out that the portion corresponding to the bulk transport shifted to frequencies that are too high to measure with the impedance analyzer, so only the inclined tail was used to obtain the conductivity values [40]. The total conductivity was calculated to be 8.2, 8.7, 5.1, and 3.2 mS cm^{-1} for LPSC, LPSC-10, LPSC-20, and LPSC-30, respectively. The temperature-dependent EIS plots (shown in Figure S4) were measured at a temperature range of 303-353 K with an interval of 5 K. As shown in Figure 2b, the activation energy was calculated to be 0.20, 0.18, 0.21, and 0.21 eV, for LPSC, LPSC-10, LPSC-20, and LPSC-30, respectively. The optimized ionic conductivity can reach 8.7 mS cm^{-1} with the activation energy of 0.18 eV when the Sn-O substitution percentage is 10%. The superior ion conduction could be attributed to the following two reasons: 1) In the pristine chlorine-rich LPSC system, the substitution of monovalent Cl$^-$ to divalent S^{2-} weakens the interactions between Li$^+$ ions and the surrounding framework anions, increases the Cl$^-$/S^{2-} site disorder and lithium vacancies, and thus enhances the Li$^+$ transport [28b, 41]. 2) The aliovalent substitution of the large-size Sn^{4+} to P^{5+} further induces the Cl$^-$/S^{2-} site disorder, expands the Li$^+$ transport channel, and consequently lowers the activation energy [19-20, 35, 40]. In addition, when the Sn-O substitution level exceeds 10%, impurity phases of Li$_4$SnS$_4$ and LiCl will form (Figure 1a), which reduces the ionic conductivity. Li$_4$SnS$_4$ was reported to possess a rather low ionic conductivity of 0.07 mS cm^{-1} at room temperature [18]. And the detrimental effect of the residual LiCl on the ionic conductivity was reported by

Peng, et al [28a]. It is also worth noting that the incorporation of oxygen in sulfides usually compromises ionic conductivity [17, 27b]. As a result, the dual-substituted LPSC-20 and LPSC-30 exhibit an ionic conductivity drop and an activation energy rise as shown in Figure 2b.

To study the effect of the sintering temperature on the ionic conductivity, solid-state sintering was carried out at 470, 500, and 530 °C. As shown in Figure 2c, all compositions exhibit optimal ionic conductivities at the sintering temperature of 500 °C. Interestingly, beside the inclined tail, an arc or a semicircle was observed for the dual-substituted samples that sintered at 530 °C as shown in Figure S5. This is assigned to the contribution of the grain boundaries that enlarges the total resistance [30, 42]. Taking the unsubstituted LPSC as an example, the phase formation under various sintering temperatures was studied by the powder XRD and the results are depicted in Figure S6. At the high sintering temperature of 530 °C, the diffraction peaks of the LiCl and Li_2S [35], two main raw materials, are detected. This could be ascribed to the loss of P_2S_5, whose boiling point is only 514 °C, at 530 °C, which leads to the incomplete reaction of the starting materials, and thus severely impairs the ionic conductivity. Comparatively, at the low sintering temperature of 470 °C, only LiCl and fewer impurities are monitored, which suggests an incomplete reaction due to insufficient diffusion of the raw materials.
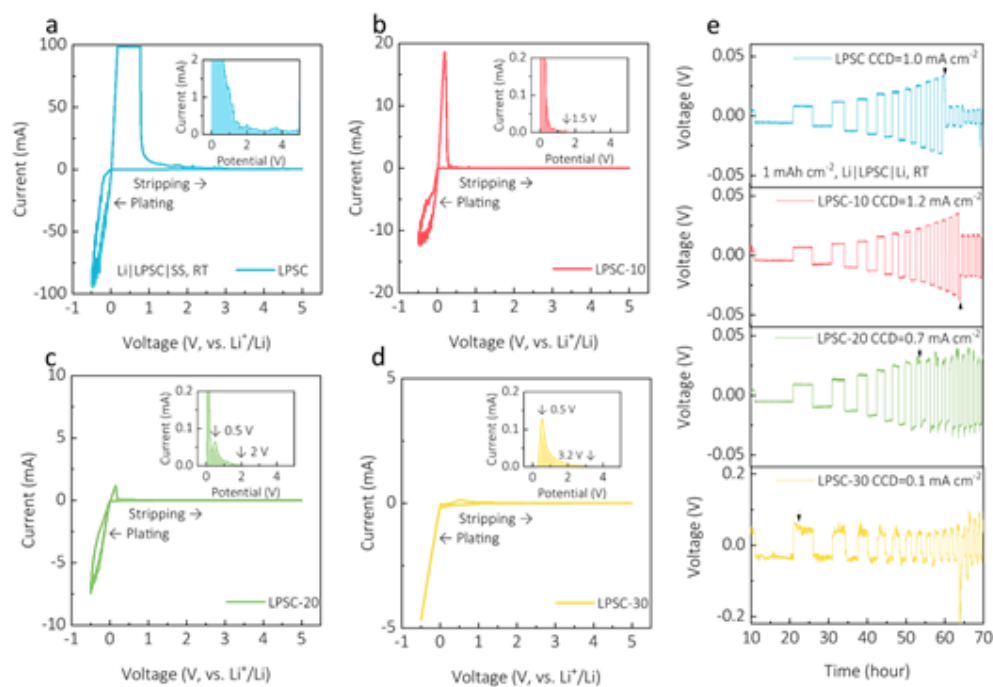
Figure 3. Lithium-anode compatibility of the sulfide samples sintered at 500 ℃. The cyclic voltammetry plots of the asymmetric Li|SE|SS cells: (a) LPSC; (b) LPSC-10; (c) LPSC-20; (d) LPSC-30. (e) The voltage profiles of the symmetric Li|SE|Li cells for the galvanostatic test. Employing the increased step size current density (0.1 mA cm^{-2}) to obtain CCD values, where the cut-off capacity of each step is fixed as 1 mAh cm^{-2}.

The electrochemical stability of solid electrolytes with lithium metal is pivotal to accomplishing lithium-metal batteries of high energy density. To survey the lithium-anode compatibility, the sulfide samples were assembled into Li|SE|SS cells for cyclic voltammetry (CV) measurements. As depicted in Figure 3a, the large cathodic and anodic currents nearby 0 V (vs. Li$^+$/Li) correspond to the lithium plating and stripping process. During the positive scan in the range of 0 - 2 V, the anodic current is so high that it exceeds 100 mA, the current

limit of the CHI600D workstation, suggesting that the unsubstituted sample has a significant decomposition in this voltage range. By contrast, the LPSC-10 shown in Figure 3b displays lithium stripping current in the range of 0 - 1.5 V and no decomposition current beyond 1.5 V up to 5 V, implying its superior compatibility with lithium anode. For LPSC-20, beside the lithium stripping current peak near 0 V, a new anodic current peak at 0.5 V is observed (Figure 3c); whereas for LPSC-30, only the current peak at 0.5 V can be seen. This hysteretic anodic current at 0.5 V is mainly associated with other lithium stripping processes, possibly resulting from the secondary phase Li_4SnS_4 of poor conductivity [18, 43] or the partly reduced Sn to form lithium-alloy [30, 44], which requires overpotential for lithium dissolution. Moreover, it can be noticed that the hysteretic current has a wider distribution (to 3.2 V) for LPSC-30 than that for LPSC-20, also related to more amount of the Sn-containing phase.

The Li|SE|Li symmetric cells were fabricated and subject to galvanostatic cycling to investigate the Li|SE interfacial stability. As depicted in Figure 3e, the voltage profiles reveal a linear growth with the ramping current densities until the voltage abruptly drops, indicating short circuits occur. The corresponding current density is called critical current density (CCD). CCD values reflect the maximum current density that an electrolyte can withstand before shorting and are thereby used to evaluate the capability of suppressing lithium dendrite growth [24-25, 45]. Table S2 has summarized the CCD and long-term cycling results from different sulfide-based symmetric lithium cells. Here, the CCD values were determined to be 1.0, 1.2, 0.7 and 0.1 mA cm^{-2}, for LPSC, LPSC-10, LPSC-20, and LPSC-30, respectively. The LPSC-10 delivers the highest CCD values as well as good reversibility in the CV results, indicating that proper Sn and O dual-substitution enables a stable and reversible Li|SE interface. However, excessive formation of secondary phase, e.g. Li_4SnS_4, in LPSC-20 and

14

LPSC-30 will cause side reactions and impair the interfacial stability, leading to irreversibility in the CV tests and noisy fluctuations of the voltage profile in the CCD tests.
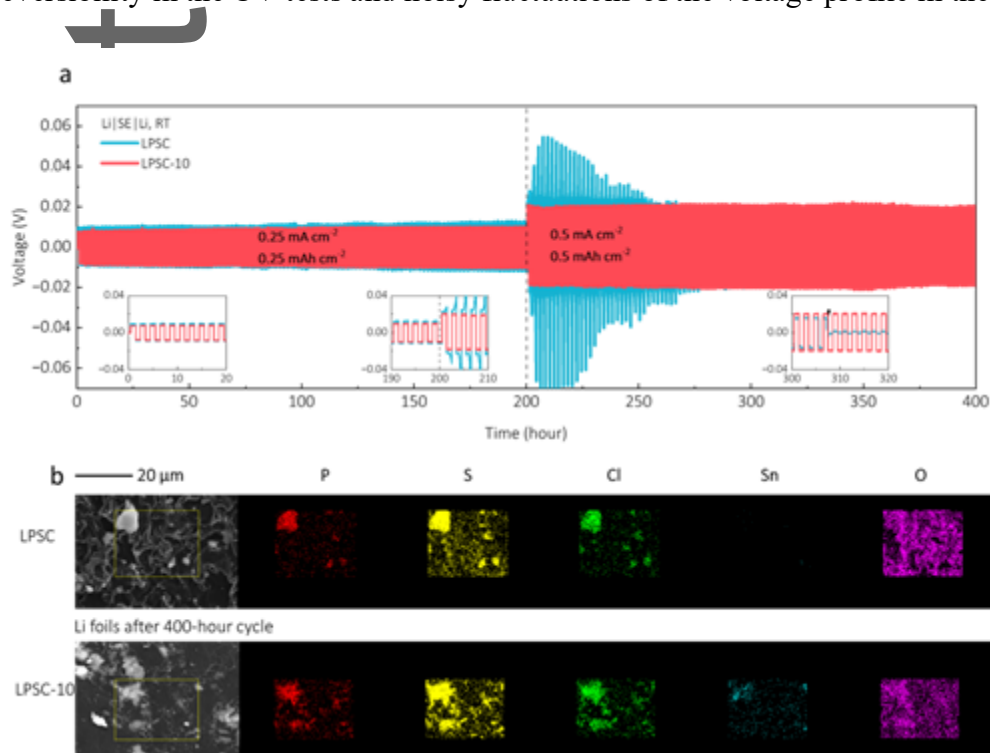

Figure 4. Long-term galvanostatic cycling stability. (a) Symmetric lithium cells cycled at 0.25 and 0.5 mA cm^{-2}. (b) The surficial morphology and element distribution of the lithium foil separated from the symmetric lithium cells after 400-hour cycling.

The long-term interfacial stability of the sulfide samples was evaluated by galvanostatically cycling the symmetric lithium cells. The voltage profiles of the symmetric cells with LPSC and LPSC-10 are depicted in Figure 4a. At a current density of 0.25 mA cm^{-2}, the Li|LPSC|Li and Li|LPSC-10|Li cells exhibit a small polarization of 9 mV (36 Ω cm^{-2}) and 8 mV (32 Ω cm^{-2}) in the initial cycle, and a slightly-increased polarization of 12 mV (48 Ω cm^{-2}) and 10 mV (40 Ω cm^{-2}) in the 100th cycle. However, when the current density is raised to 0.5 mA cm^{-2}, the polarization of Li|LPSC|Li sharply increases as the inset

shows, and then gradually decreases before it abruptly drops to nearly 0 after nearly 300 hours, indicating the occurrence of short circuit in the Li|LPSC|Li [21]. In contrast, Li|LPSC-10|Li still maintains a stable polarization of about 20 mV (40 Ω cm^{-2}) at 0.5 mA cm^{-2} after 400 hours, demonstrating its enhanced lithium-anode compatibility and electrochemical stability.

The lithium foils separated from the symmetric lithium cells after 400-hour cycling were subject to morphology observation. As shown in Figure 4b, some sulfide particles remain on the lithium matrix after the immersion treatment in the toluene. According to the EDS mapping, P, S, Cl, and Sn elements are mainly detected from the sulfide particles. However, O elements are distributed on the whole detected area, suggesting the oxidation of the lithium matrix during the short-time air exposure when the sample was transferred into the vacuum chamber of the SEM. The as-cycled lithium matrix in the Li|LPSC|Li and Li|LPSC-10|Li cells distinctly differ in morphology, whose details can be seen in Figure S7. It can be seen that the lithium separated from the Li|LPSC|Li cell looks like a porous network [35], indicating uneven plating and stripping due to the lithium-anode incompatibility, which eventually causes cell failure. As a comparison, the lithium separated from the Li|LPSC-10|Li cell looks dense and relatively smooth, suggesting that the Sn and O dual-substituted sulfide electrolyte enables the stable plating and stripping process.

To shed light on the interface evolution between the lithium anode and sulfide electrolyte during lithium deposition/stripping, XPS measurement was performed to obtain the chemical information on the lithium foils and electrolyte. To accelerate the interfacial reaction, the symmetric lithium cells was cycled at a current density of 0.5 mA cm^{-2} at 65 °C. As depicted in Figure S8, the binding energy for P, S and Sn elements agrees well with the reported literatures [7, 30, 44a, 46] for the pristine LPSC and LPSC-10 samples. After 10 cycles, some

reduced species like Li_3P and Li_2S were detected in the Li|LPSC interface, indicating the decomposition reaction of sulfide electrolyte with lithium anode [4a]. The Li_2S content in atomic ratio decreases from 21.8% for Li|LPSC to 10.9% for Li|LPSC-10, suggesting the improved stability with the dual-substitution of Sn and O elements. Moreover, the existence of oxysulfide like PS_3O^{3-} as shown in Figure 8c increases the chemical stability against lithium anode [16, 27b] and thus avoids higher degree of decomposition. Meanwhile, part of Sn^{4+} ion is reduced to form Li-Sn alloy as shown in Figure S8e, which is beneficial to the uniform lithium deposition and stripping at the interface [30]. Furthermore, another batch of symmetric lithium cells with LPSC and LPSC-10 were galvanostatically cycled under the same condition for 50 cycles and subject to the EIS measurement before and after cycling. As shown in Figure S9b,c, both cells before cycling exhibit low interfacial resistance, 118.8 Ohm cm and 90.1 Ohm cm for LPSC and LPSC-10, respectively. However, the polarization voltage of Li|LPSC|Li continuously increases over 100 hours, after which the interfacial resistance increases to 5204 Ohm cm. In contrast, the Li|LPSC-10|Li remarkably maintains a low interfacial resistance. After 100-hour cycling, the interfacial resistance even slightly decreases to 62.0 Ohm cm, which is due to the in-situ formed Li-Sn alloy interphase of the dual-substituted sample.
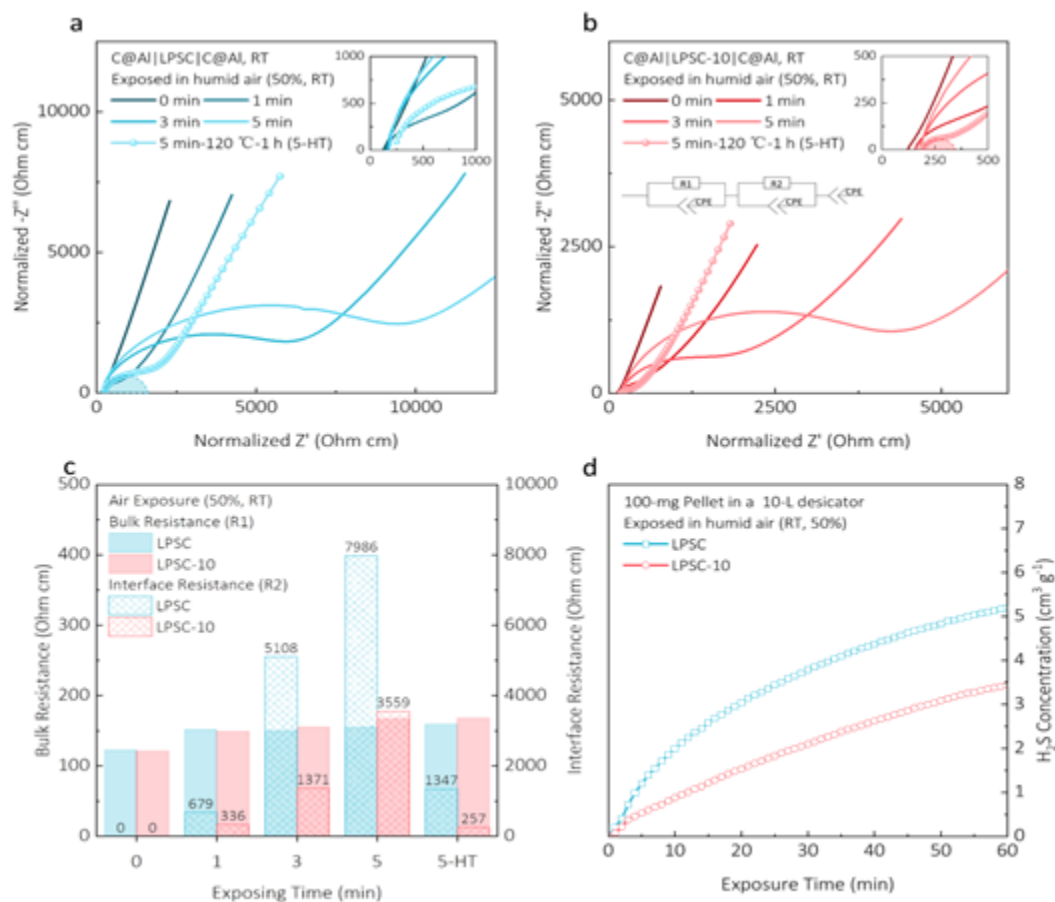
17

Figure 5. Moisture stability comparison of LPSC and LPSC-10 in the air atmosphere with a relative humidity of 50%. Nyquist plots for (a) LPSC; (b) LPSC-10 after air exposure with different times (0, 1, 3, 5 min) and heat treatment (5-HT, tempering at 120 °C for 1 hour for the 5-minute-exposure samples). (c) The bulk resistance (R1) and interface resistance (R2) for the sulfide samples in the air-exposure test. (d) The monitored H_2S concentration versus air-exposure time.

Sulfide electrolyte generally suffers from reactions with the moisture in the air during production and storage, resulting in the deterioration of the ionic conductivity and the

generation of toxic H_2S gas. Therefore, the humid-air-exposed tests were carried out to assess the moisture tolerance of the samples. The EIS plots of the air-exposed LPSC and LPSC-10 samples are depicted in Figures 5a and 5b. A semicircle appears in the high-frequency region in the EIS plots as a result of air exposure, meaning the total resistance increases [40]. This can be attributed to the reaction of H_2O with the surficial layer of the cold-pressed pellet, leading to the degradation of the samples. Moreover, the radius of the semicircle grows with an exposure time of up to 5 minutes, indicating that the surface reaction is not self-inhibiting.

To quantitatively analyze the resistance of the surficial reaction layer, an equivalent circuit of (R1//CPE)-(R2//CPE)-CPE was employed to fit the EIS plots [4a], where R1 and R2 refer to the bulk resistance and interfacial resistance, respectively. The fitted results are shown in Figure 5c. The bulk resistance, R1, slightly increases but remains the same magnitude during the exposure. By contrast, the interfacial resistance, R2, increases significantly with the exposure time for both LPSC and LPSC-10. For example, the R2 of the LPSC increases from 0 to 7986 Ω cm after 5-minute exposure. However, LPSC-10 invariably maintains a lower R2 value, half less than that of LPSC, implying that the dual-substituted LPSC-10 has better moisture stability. To exclude the impact of the physically-absorbed water, the 5-minute-exposed samples were tempered at 120 °C for 1 hour (labeled as 5-HT) and subject to impedance measurements. As shown in Figure 5c, after heat treatment, R2 reduces to 1347 Ω cm from 7986 Ω cm for LPSC, whereas R2 reduces to 257 Ω cm from 3559 Ω cm, suggesting that simple heat treatment can help relieve the surface deterioration. Besides, the 5-HT samples were assembled into symmetric lithium cells for galvanostatic cycling. As shown in Figure S10, for Li|LPSC(5-HT)|Li, the polarization voltage presents sharp fluctuation during the lithium plating/stripping process and the maximum voltage is up to 40 mV (400 Ω cm^{-2}) at a current density of 0.1 mA cm^{-2}. When the current density is raised
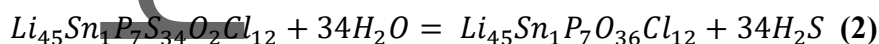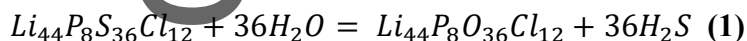
19

to 0.2 mA cm^{-2}, the polarization voltage turns extremely unstable and the cell finally fails in several cycles. In sharp contrast to this, the Li|LPSC-10(5-HT)|Li cell has a rather stable voltage profile at 0.1 mA cm^{-2} and can withstand the current density of 0.2 mA cm^{-2} over 300-hour cycling, which can be attributed to the low interfacial resistance of LPSC-10(5-HT).

Furthermore, the structure stability of the samples was examined by scrutinizing the X-ray diffraction [27a, 47]. As displayed in Figure S11a, the air-exposed and heat-treated samples exhibit similar diffraction patterns with slightly-reduced intensity compared with the pristine one. However, certain amount of LiCl was detected for both the air-exposed and heat-treated samples. This indicates the irreversible degradation occurred [35], explaining that the extra resistance of air-exposed samples can be reduced by simple heat treatment but cannot be eliminated as depicted in Figure 5c. Compared with LPSC-10(5-HT), the significant difference is that the diffraction peaks spotted at 52.7° ($2\theta_1$) and 52.88° ($2\theta_2$) in LPSC(5-HT) becomes abnormally sharp and split. The split peaks originate from the Cu K$_{\alpha1}$ and K$_{\alpha2}$ lines at high diffraction angles [48] since the $\sin(2\theta_1)/\sin(2\theta_2)$ very close to the wavelength ratio of Cu K$_{\alpha1}$ (1.54056 Å) and K$_{\alpha2}$ (1.54439 Å) used in actual measurement. And the abnormal intensity may result from the preferred orientation of a certain crystalline plane (hkl = 440) during the tempering process, indicating the stronger absorption of moisture and weaker stability against moisture for the unsubstituted LPSC.

In addition to the electrochemical measurement, H$_2$S gas concentration was monitored when the pelletized sample was exposed to humid air in an airtight container [49]. As shown in Figure 5d, during one-hour exposure, both LPSC and LPSC-10 release H$_2$S gas, and the concentration gradually rises. The H$_2$S concentration after 1-hour exposure is determined to be 5.2 and 3.4 cm^3 g^{-1} for LPSC and LPSC-10, respectively. Raman spectroscopy measurement was conducted to further analyze the impact of moisture to the structure of

sulfide electrolyte. As shown in Figure S11, for the unsubstituted LSPC, the air-exposed sample exhibits significantly-reduced intensity of PS_4^{3-} (429 cm^{-1}) for all the three vibration modes, and the heat-treated sample could not return to its pristine state. However, no evidence of PO_4^{3-} at 950 cm^{-1} is found [47], mainly because the degree of O replacing S was not enough with one-hour exposure. By comparison, both the air-exposed and heat-treated samples of LPSC-10 exhibit slightly-reduced intensity of PS_4^{3-} vibration (429 cm^{-1}) and the intensity of SnS_4^{4-} vibration (346 cm^{-1}) was basically the same as that of the pristine sample. PO_4^{3-} at 950 cm^{-1} is mainly from the O substitution; the air exposure did not increase the intensity of PO_4^{3-} vibration for LPSC-10. The smaller amount of H_2S gas generated from LPSC-10 and less structure degradation illustrate that the incorporation of Sn and O elements will enhance the tolerance against the H_2O of the chlorine-rich argyrodite.

The first-principles calculation was employed to study the hydrolysis energy (ΔG) of the reaction between the chlorine-rich argyrodite and H_2O [19-20]. The detailed reactions of the pristine and the dual-substituted one are listed in equations 1 and 2. ΔG for them are determined to be -0.48 and -0.40 eV/H_2O, respectively. The higher ΔG value means that the hydrolysis reaction is more difficult for the dual-substituted structure, in agreement with the experimental observation. The calculation results well explain that the dual-substituted sample is less vulnerable to moisture, produces less amount of H_2S gas, and exhibits lower resistance and better cycling in the electrochemical tests.
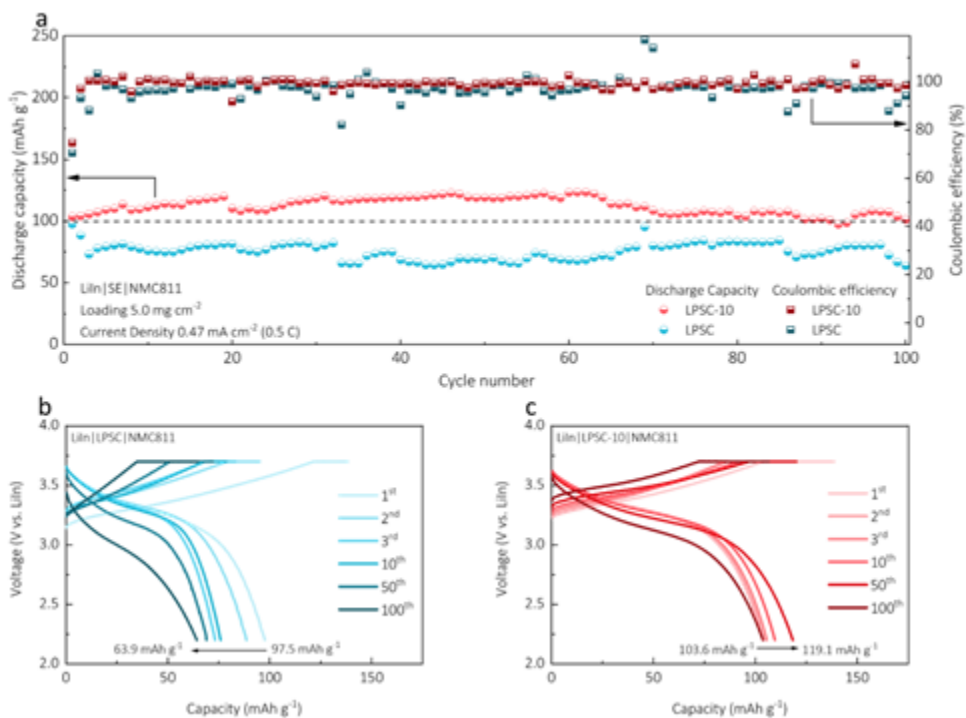
$$Li_{44}P_8S_{36}Cl_{12} + 36H_2O = Li_{44}P_8O_{36}Cl_{12} + 36H_2S \quad \textbf{(1)}$$

$$Li_{45}Sn_1P_7S_{34}O_2Cl_{12} + 34H_2O = Li_{45}Sn_1P_7O_{36}Cl_{12} + 34H_2S \quad \textbf{(2)}$$

Figure 6. Electrochemical performance of the LiIn|SE|NMC811 cells at 38 ± 2 ^{o}C with a holding pressure of 5 MPa. (a) Cycling performance for 100 cycles at 0.5 C rate. The corresponding voltage profiles at different cycles (1st, 2nd, 3rd, 10th, 50th, 100th): (b) LiIn|LPSC|NMC811; (c) LiIn|LPSC-10|NMC811.

To evaluate the electrochemical performance of the sulfide electrolyte, particularly the compatibility with Ni-rich cathodes, LPSC and LPSC-10 were paired with $LiNi_{0.8}Mn_{0.1}Co_{0.1}O_2$ cathode and Li-In anode to assemble into ASSLBs. The assembled batteries were galvanostatically cycled within 2.2-3.7 V vs Li-In alloy (2.8-4.3 V vs Li^+/Li) at the rate of 0.5 C (0.47 mA cm^{-2}). As shown in Figure 6a, both cells have been successfully cycled for 100 cycles. However, the electrochemical performance differs a lot in terms of the discharge capacity. Specifically, the initial discharge capacity of LiIn|LPSC|NMC811 and LiIn|LPSC-10|NMC811 is 97.5 and 103.6 mAh g^{-1}, respectively, corresponding to the initial

22

coulombic efficiency of 70.5% and 74.7%. After 100 cycles, the discharge capacity of the battery employing LPSC decays to 63.9 mAh g^{-1} with a capacity retention rate of 65.5%; in contrast, the discharge capacity of the battery employing LPSC-10 is 101.4 mAh g^{-1} and the capacity retention rate is as high as 97.9%. Accordingly, the coulombic efficiency of LiIn|LPSC-10|NMC811 exhibits less fluctuation throughout the test than that of LiIn|LPSC|NMC811, suggesting a more stable electrolyte|cathode interface with LPSC-10.

The voltage profiles in different cycles are depicted in Figures 6b and 6c. For LiIn|LPSC|NMC811, the discharge capacity rapidly decays from 97.5 to 73.2 mAh g^{-1} during the first three cycles, suggesting poor compatibility in the composite cathode [50]. The discharge capacity in the 10th, 50th, and 100th cycle is 75.9, 69.0, and 63.9 mAh g^{-1}, respectively. It can be inferred that most of the capacity loss mainly happens in the initial cycles. Besides, the ever-increasing polarization of the battery not only causes the discharge capacity to further decline but also impairs the energy and power density. Comparatively, for the battery employing LPSC-10, the discharge capacity in the 1st, 2nd, 3rd, 10th, 50th, and 100th cycles is 103.6, 104.2, 105.6, 111.3, 119.1, and 101.4 mAh g^{-1}, respectively. During the first 50 cycles, the discharge capacity for LiIn|LPSC-10|NMC811 slightly increases, which might be attributed to the gradual improvement of the interfacial contact between the sulfide electrolytes and the active materials in the composite cathode. On the whole, the steady release of the discharge capacity benefits from the smaller change of the voltage polarization. The excellent electrochemical performance of the LiIn|LPSC-10|NMC811 battery suggests that the incorporation of Sn and O elements in the chlorine-rich argyrodite will improve the compatibility with the Ni-rich cathode and subsequently provide good cycling stability.

23

3. Conclusions

Chlorine-rich argyrodite-type sulfide is a promising electrolyte material with ultrahigh ionic conductivity for all-solid-state lithium-ion batteries, but obstructed by its poor resistivity to moisture and dissatisfactory electrochemical stability. Sn and O dual-substitution strategy was propounded in this work to ease the moisture sensitivity and boost the interfacial stability simultaneously. $Li_{5.4+x}(P_{1-x}Sn_x)(S_{4.4-2x}O_{2x})Cl_{1.6}$ (x = 0, 0.1, 0.2, and 0.3) were successfully synthesized via solid state sintering. XRD and Raman measurements demonstrate a decent amount of Sn and O atoms will embed into the lattice and thiophosphate unit, and the excess amount of Sn exists in the formation of Li_4SnS_4. The systematic optimization over sintering temperature and substitution amount determines $Li_{5.5}(P_{0.9}Sn_{0.1})(S_{4.2}O_{0.2})Cl_{1.6}$ (LPSC-10) sintered at 500 °C exhibits the best ionic conductivity of 8.7 mS cm^{-1}, the most stable lithium plating/striping with an electrochemical window up to 5 V, and the highest tolerance of lithium dendrites with a critical current density of 1.2 mA cm^{-2}. The symmetric lithium cell assembled with LPSC-10 was cycled at 0.5 mA cm^{-2} for 200 hours, and the as-cycled lithium anode displays a rather regulated and dense morphology. Besides, the humid-air-exposed LPSC-10 delivers a smaller increment in total resistance, generates a mild amount of H_2S gas, and displays favorable structure stability after simple heat treatment. The as-treated LPSC-10 was integrated into a symmetric lithium cell, which stably cycled at 0.2 mA cm^{-2} for 300 hours. The DFT calculation also confirms that the dual-substituted model has a lower tendency of hydrolysis. The full battery fabricated with LPSC-10 and LiIn|NMC811 electrodes presents a high initial discharge capacity of 103.6 mAh g^{-1} at 0.5 C rate and maintains 101.4 mAh g^{-1} at the 100th cycle, with a 97.9% capacity retention rate. In summary, the Sn and O dual substitution strategy in chlorine-rich argyrodites will facilitate the development practices on all-solid-state lithium batteries.

Supporting Information

Supporting Information is available from the Wiley Online Library or from the author.

Acknowledgments

Received: ((will be filled in by the editorial staff))

Revised: ((will be filled in by the editorial staff))

Published online: ((will be filled in by the editorial staff))

References

[1]   a) J. C. Bachman, S. Muy, A. Grimaud, H.-H. Chang, N. Pour, S. F. Lux, O. Paschos, F. Maglia, S. Lupart, P. Lamp, L. Giordano, Y. Shao-Horn, *Chemical Reviews* **2016**, 116, 140; b) Z. Zhang, Y. Shao, B. Lotsch, Y.-S. Hu, H. Li, J. Janek, L. F. Nazar, C.-W. Nan, J. Maier, M. Armand, L. Chen, *Energy & Environmental Science* **2018**, 11, 1945; c) K. J. Kim, M. Balaish, M. Wadaguchi, L. Kong, J. L. M. Rupp, *Advanced Energy Materials* **2021**, 11, 2002689.

[2]   a) Y. Seino, T. Ota, K. Takada, A. Hayashi, M. Tatsumisago, *Energy Environ. Sci.* **2014**, 7, 627; b) N. Kamaya, K. Homma, Y. Yamakawa, M. Hirayama, R. Kanno, M. Yonemura, T. Kamiyama, Y. Kato, S. Hama, K. Kawamoto, A. Mitsui, *Nat Mater* **2011**, 10, 682; c) Y. Kato, S. Hori, T. Saito, K. Suzuki, M. Hirayama, A. Mitsui, M.

Yonemura, H. Iba, R. Kanno, *Nature Energy* **2016**, 1, 16030; d) Z. Zhang, L. Wu, D. Zhou, W. Weng, X. Yao, *Nano Letters* **2021**, 21, 5233.

[3]   a) C. Wang, R. Yu, H. Duan, Q. Lu, Q. Li, K. R. Adair, D. Bao, Y. Liu, R. Yang, J. Wang, S. Zhao, H. Huang, X. Sun, *ACS Energy Letters* **2021**, 7, 410; b) Y. Li, Y. Wu, Z. Wang, J. Xu, T. Ma, L. Chen, H. Li, F. Wu, *Materials Today* **2022**, 55, 92.

[4]   a) S. Wenzel, S. J. Sedlmaier, C. Dietrich, W. G. Zeier, J. Janek, *Solid State Ionics* **2018**, 318, 102; b) S. Wenzel, S. Randau, T. Leichtweiß, D. A. Weber, J. Sann, W. G. Zeier, J. Janek, *Chemistry of Materials* **2016**, 28, 2400.

[5]   C. Yu, F. Zhao, J. Luo, L. Zhang, X. Sun, *Nano Energy* **2021**, 83, 105858.

[6]   H. J. Deiseroth, S. T. Kong, H. Eckert, J. Vannahme, C. Reiner, T. Zaiss, M. Schlosser, *Angew Chem Int Ed Engl* **2008**, 47, 755.

[7]   D. Zeng, J. Yao, L. Zhang, R. Xu, S. Wang, X. Yan, C. Yu, L. Wang, *Nature Communications* **2022**, 13, 1909.

[8]   P. Lu, D. Wu, L. Chen, H. Li, F. Wu, *Electrochemical Energy Reviews* **2022**, 5, 3.

[9]   X. Bai, Y. Duan, W. Zhuang, R. Yang, J. Wang, *Journal of Materials Chemistry A* **2020**, 8, 25663.

[10]   Y. Zhu, X. He, Y. Mo, *ACS Appl Mater Interfaces* **2015**, 7, 23685.

[11]   C. Yu, L. van Eijck, S. Ganapathy, M. Wagemaker, *Electrochimica Acta* **2016**, 215, 93.

[12]   Y. Liang, H. Liu, G. Wang, C. Wang, Y. Ni, C.-W. Nan, L.-Z. Fan, *InfoMat* **2022**, 4, 12292.

[13]   Z. Ning, D. S. Jolly, G. Li, R. De Meyere, S. D. Pu, Y. Chen, J. Kasemchainan, J. Ihli, C. Gong, B. Liu, D. L. R. Melvin, A. Bonnin, O. Magdysyuk, P. Adamson, G. O. Hartley, C. W. Monroe, T. J. Marrow, P. G. Bruce, *Nat Mater* **2021**, 20, 1121.

[14] a) J. Zhang, C. Zheng, L. Li, Y. Xia, H. Huang, Y. Gan, C. Liang, X. He, X. Tao, W. Zhang, *Advanced Energy Materials* **2019**, 10, 1903311; b) F. Walther, R. Koerver, T. Fuchs, S. Ohno, J. Sann, M. Rohnke, W. G. Zeier, J. Janek, *Chemistry of Materials* **2019**, 31, 3745.

[15] D. Lee, K.-H. Park, S. Y. Kim, J. Y. Jung, W. Lee, K. Kim, G. Jeong, J.-S. Yu, J. Choi, M.-S. Park, W. Cho, *Journal of Materials Chemistry A* **2021**, 9, 17311.

[16] H. Xu, G. Cao, Y. Shen, Y. Yu, J. Hu, Z. Wang, G. Shao, *ENERGY & ENVIRONMENTAL MATERIALS* **2022**, 5, 852.

[17] Z. Zhang, L. Zhang, X. Yan, H. Wang, Y. Liu, C. Yu, X. Cao, L. van Eijck, B. Wen, *Journal of Power Sources* **2019**, 410-411, 162.

[18] G. Sahu, Z. Lin, J. Li, Z. Liu, N. Dudney, C. Liang, *Energy & Environmental Science* **2014**, 7, 1053.

[19] F. Zhao, J. Liang, C. Yu, Q. Sun, X. Li, K. Adair, C. Wang, Y. Zhao, S. Zhang, W. Li, S. Deng, R. Li, Y. Huang, H. Huang, L. Zhang, S. Zhao, S. Lu, X. Sun, *Advanced Energy Materials* **2020**, 10, 1903422.

[20] Z. Jiang, H. Peng, Y. Liu, Z. Li, Y. Zhong, X. Wang, X. Xia, C. Gu, J. Tu, *Advanced Energy Materials* **2021**, 11, 2101521.

[21] L. Ye, X. Li, *Nature* **2021**, 593, 218.

[22] Y.-G. Lee, S. Fujiki, C. Jung, N. Suzuki, N. Yashiro, R. Omoda, D.-S. Ko, T. Shiratsuchi, T. Sugimoto, S. Ryu, J. H. Ku, T. Watanabe, Y. Park, Y. Aihara, D. Im, I. T. Han, *Nature Energy* **2020**, 5, 299.

[23] Y. Liu, H. Su, M. Li, J. Xiang, X. Wu, Y. Zhong, X. Wang, X. Xia, C. Gu, J. Tu, *Journal of Materials Chemistry A* **2021**, 9, 13531.

[24] F. Zhao, Q. Sun, C. Yu, S. Zhang, K. Adair, S. Wang, Y. Liu, Y. Zhao, J. Liang, C. Wang, X. Li, X. Li, W. Xia, R. Li, H. Huang, L. Zhang, S. Zhao, S. Lu, X. Sun, *ACS Energy Letters* **2020**, 5, 1035.

[25]   F. Han, J. Yue, X. Zhu, C. Wang, *Advanced Energy Materials* **2018**, 8, 1703644.

[26]   X. Fan, X. Ji, F. Han, J. Yue, J. Chen, L. Chen, T. Deng, J. Jiang, C. Wang, *Science Advances* 4, 9245.

[27]   a) L. Ye, E. Gil-González, X. Li, *Electrochemistry Communications* **2021**, 128, 107058; b) L. Peng, S. Chen, C. Yu, C. Wei, C. Liao, Z. Wu, H. L. Wang, S. Cheng, J. Xie, *ACS Appl Mater Interfaces* **2022**, 14, 4179.

[28]   a) L. Peng, C. Yu, Z. Zhang, H. Ren, J. Zhang, Z. He, M. Yu, L. Zhang, S. Cheng, J. Xie, *Chemical Engineering Journal* **2022**, 430, 132896; b) P. Adeli, J. D. Bazak, K. H. Park, I. Kochetkov, A. Huq, G. R. Goward, L. F. Nazar, *Angewandte Chemie International Edition* **2019**, 58, 8681.

[29]   T. Kaib, S. Haddadpour, M. Kapitein, P. Bron, C. Schröder, H. Eckert, B. Roling, S. Dehnen, *Chemistry of Materials* **2012**, 24, 2211.

[30]   T. Chen, D. Zeng, L. Zhang, M. Yang, D. Song, X. Yan, C. Yu, *Journal of Energy Chemistry* **2021**, 59, 530.

[31]   T. Chen, L. Zhang, Z. Zhang, P. Li, H. Wang, C. Yu, X. Yan, L. Wang, B. Xu, *ACS Applied Materials & Interfaces* **2019**, 11, 40808.

[32]   L. Sang, R. T. Haasch, A. A. Gewirth, R. G. Nuzzo, *Chemistry of Materials* **2017**, 29, 3029.

[33]   K. Kanazawa, S. Yubuchi, C. Hotehama, M. Otoyama, S. Shimono, H. Ishibashi, Y. Kubota, A. Sakuda, A. Hayashi, M. Tatsumisago, *Inorganic Chemistry* **2018**, 57, 9925.

[34]   L. Popović, B. Manoun, D. de Waal, M. K. Nieuwoudt, J. D. Comins, *Journal of Raman Spectroscopy* **2003**, 34, 77.

[35]   B. W. Taklu, W.-N. Su, Y. Nikodimos, K. Lakshmanan, N. T. Temesgen, P.-X. Lin, S.-K. Jiang, C.-J. Huang, D.-Y. Wang, H.-S. Sheu, S.-H. Wu, B. J. Hwang, *Nano Energy* **2021**, 90, 106542.

28

[36]   R. Hu, Y. Ouyang, T. Liang, H. Wang, J. Liu, J. Chen, C. Yang, L. Yang, M. Zhu, *Advanced Materials* **2017**, 29, 1605006.

[37]   A. Sakuda, A. Hayashi, M. Tatsumisago, *Current Opinion in Electrochemistry* **2017**, 6, 108.

[38]   J. T. S. Irvine, D. C. Sinclair, A. R. West, *Advanced Materials* **1990**, 2, 132.

[39]   a) N. Minafra, S. P. Culver, T. Krauskopf, A. Senyshyn, W. G. Zeier, *Journal of Materials Chemistry A* **2018**, 6, 645; b) M. A. Kraft, S. P. Culver, M. Calderon, F. Böcher, T. Krauskopf, A. Senyshyn, C. Dietrich, A. Zevalkink, J. Janek, W. G. Zeier, *Journal of the American Chemical Society* **2017**, 139, 10909.

[40]   M. A. Kraft, S. Ohno, T. Zinkevich, R. Koerver, S. P. Culver, T. Fuchs, A. Senyshyn, S. Indris, B. J. Morgan, W. G. Zeier, *Journal of the American Chemical Society* **2018**, 140, 16330.

[41]   N. J. J. de Klerk, I. Rosłoń, M. Wagemaker, *Chemistry of Materials* **2016**, 28, 7955.

[42]   C. Yu, S. Ganapathy, E. R. H. van Eck, L. van Eijck, S. Basak, Y. Liu, L. Zhang, Henny W. Zandbergen, M. Wagemaker, *Journal of Materials Chemistry A* **2017**, 5, 21178.

[43]   M. Otoyama, K. Kuratani, H. Kobayashi, *Ceramics International* **2021**, 47, 28377.

[44]   a) Y. Li, J. Li, J. Cheng, X. Xu, L. Chen, L. Ci, *Advanced Materials Interfaces* **2021**, 8, 2100368; b) R. Z. Hu, Y. Zhang, M. Zhu, *Electrochimica Acta* **2008**, 53, 3377; c) C. Chang, L. Liu, S. Wang, L. Li, X. Liu, *Metallurgical and Materials Transactions A* **2018**, 49, 5930.

[45]   H. Zheng, S. Wu, R. Tian, Z. Xu, H. Zhu, H. Duan, H. Liu, *Advanced Functional Materials* **2020**, 30, 1906189.

[46]   Y. Liu, H. Su, Y. Zhong, X. Wang, X. Xia, C. Gu, J. Tu, *Advanced Functional Materials* **2022**, 32, 2207978.

[47]   P. Lu, L. Liu, S. Wang, J. Xu, J. Peng, W. Yan, Q. Wang, H. Li, L. Chen, F. Wu, *Advanced Materials* **2021**, 33, 2100921.

[48]   K. D. M. Harris, in *Advanced X-Ray Crystallography*, DOI: 10.1007/128_2011_251 (Ed: K. Rissanen), Springer Berlin Heidelberg, Berlin, Heidelberg **2012**, p. 133.

[49]   a) A. Hayashi, H. Muramatsu, T. Ohtomo, S. Hama, M. Tatsumisago, *Journal of Materials Chemistry A* **2013**, 1, 6320; b) H. Muramatsu, A. Hayashi, T. Ohtomo, S. Hama, M. Tatsumisago, *Solid State Ionics* **2011**, 182, 116.

[50]   J. Auvergniot, A. Cassel, J.-B. Ledeuil, V. Viallet, V. Seznec, R. Dedryvère, *Chemistry of Materials* **2017**, 29, 3883.

By introducing Sn and O dual substitution in chlorine-rich argyrodite $Li_{5.4}PS_{4.4}Cl_{1.6}$, and comparing the different substitution levels, $Li_{5.5}(P_{0.9}Sn_{0.1})(S_{4.2}O_{0.2})Cl_{1.6}$ is demonstrated to possess the enhanced moisture stability, exhibit the dendrite-free lithium stripping/plating at 0.5 mA cm^{-2}, and enable high capacity retention of 97.9% at 0.5 C rate (101.4 mAh g^{-1} at 100th cycle) using NMC cathode.

Guoyao Li[a], Shaoping Wu[a], Hongpeng Zheng[a], Yu Yang[b], Jingyu Cai[a], Hong Zhu[b], Xiao Huang[c], Hezhou Liu[a], Huanan Duan[a]*

[a]G. Li, S. W, H. Zheng, J. Cai, H. Liu, H. Duan*

State Key Laboratory of Metal Matrix Composites, School of Materials Science and Engineering, Shanghai Jiao Tong University, Shanghai 200240, P. R. China

E-mail: hduan@sjtu.edu.cn

[b]Y. Yang, H. Zhu

University of Michigan-Shanghai Jiao Tong University Joint Institute, Shanghai Jiao Tong University, Shanghai 200240, P. R. China

[c]X. Huang

SZU-NUS Collaborative Innovation Center for Optoelectronic Science & Technology, International Collaborative Laboratory of 2D Materials for Optoelectronics Science and Technology of Ministry of Education, Institute of Microscale Optoelectronics, Shenzhen University, Shenzhen 518060, P. R. China

Title: Sn-O Dual-substituted Chlorine-rich Argyrodite Electrolyte with Enhanced Moisture and Electrochemical Stability

ToC figure ((Please choose one size: 55 mm broad × 50 mm high **or** 110 mm broad × 20 mm high. Please do not use any other dimensions))